

## FIBRE AGGLOMERATE TRANSPORT IN A HORIZONTAL FLOW

**II. G. M. Cartland Glover, E. Krepper, H. Kryk and F.-P. Weiss,  
I2. S. Renger, A. Seeliger, F. Zacharias, A. Kratzsch, S. Alt, and W. Kästner**

*II. Institut für Sicherheitsforschung, Forschungszentrum Dresden-Rossendorf, Postfach  
510119, D-01314, Dresden, Deutschland*

*I2. Institut für Prozeßtechnik, Prozeßautomatisierung und Meßtechnik, Hochschule Zittau-  
Görlitz, Postfach 1455, D-02754, Zittau, Deutschland*

### **Abstract**

An experimental and theoretical study of the transport of mineral wool fibre agglomerates in nuclear power plant containment sumps is being performed. A racetrack channel was devised to provide data for the validation of numerical models, which are intended to model the transport of fibre agglomerates. The racetrack channel provides near uniform and steady conditions that lead to either the sedimentation or suspension of the agglomerates. Various experimental techniques were used to determine the velocity conditions and the distribution of the fibre agglomerates in the channel. The fibre agglomerates are modelled as fluid particles in the Eulerian reference frame. Simulations of pure sedimentation of a known mass and volume of agglomerations show that the transport of the fibre agglomerates can be replicated. The suspension of the fibres is also replicated in the simulations; however, the definition of the fibre agglomerate phase is strongly dependent on the selected density and diameter. Detailed information on the morphology of the fibre agglomerates is lacking for the suspension conditions, as the fibre agglomerates may undergo breakage and erosion. Therefore, ongoing work, which is described here, is being pursued to improve the experimental characterisation of the suspended transport of the fibre agglomerates.

### **1. INTRODUCTION**

Loss of coolant accidents in the primary circuit of pressure and boiling water reactors can cause the damage of insulation materials that clad adjacent structures. These materials may then find their way to the containment sump where water is drawn into the ECCS (emergency core cooling system). Strainers in the containment sump may become blocked (either partially or fully) by the insulation materials. The consequences of such blockages are an increased pressure drop acting on the operating ECCS pumps. If the strainers are partially blocked, smaller particles can also penetrate the strainers. These smaller particles can therefore enter the reactor coolant system and then may accumulate in the reactor pressure vessel. Knowledge bases and workshops (see relevant OECD and NUREG reports in the references) describe some of the research activities into the effect that debris has on the ECCS.

Note that the adequate modelling of flow phenomena in the containment sump has been considered in a single-phase reference frame in combination with probabilistic risk assessments (Detar et al 2008, Lee et al. 2008, NUREG/CR-6773, Seo et al. 2009). However, this introduces significant uncertainties into the assessment of the quantity of debris that may reach and penetrate the sump strainers. Therefore, multiphase flow models of submerged debris transport through the sump may reduce such uncertainties.

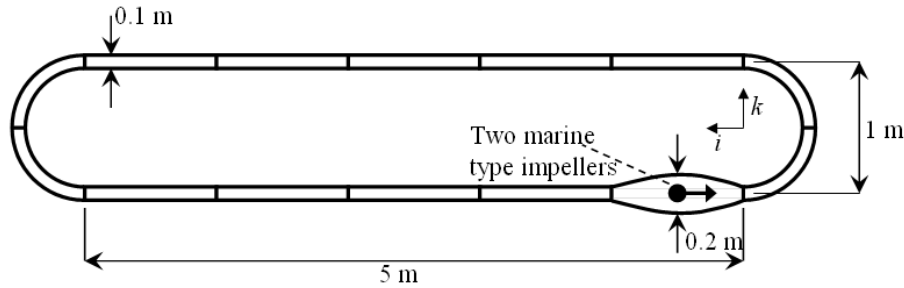


Fig. 1: Plan of the racetrack type channel; the axes lie on the origin and the vertical component is  $j$ ;

### 1.1 Joint Research Project

An experimental and theoretical study that concentrates on mineral wool fibre transport in the containment sump and the ECCS is being performed (Krepper et al. 2009). The study entails the generation of fibre agglomerates by high-pressure steam jets and the assessment of the transport of such agglomerates in single and multi-effect experiments.

The experiments include measurement of the terminal settling velocity, the strainer pressure drop, fibre sedimentation and resuspension in a channel flow, jet flow in a rectangular tank and the importance of chemical effects on any filter cake formed on the strainer. An integrated test facility is also operated to assess the compounded effects on the scale of the containment sump and any accumulation of fibres that may occur in a fuel assembly.

Each experimental facility is used to provide data for the validation of equivalent computational fluid dynamic and system models in order to develop generic models that characterise the typical phenomena in loss of coolant accidents in the reactor primary circuit (Krepper et al. 2009). The focus of the studies described here are the experiments performed in a racetrack type channel that is used to examine the sedimentation and suspension of fibre agglomerates in a horizontal flow.

## 2. EXPERIMENTAL DESCRIPTION

The measurement techniques and experimental studies performed on the flat racetrack type channel are described below.

### 2.1 Geometry

The racetrack type channel used here has a channel width of 0.1 m, a depth of 1.2m, which is filled with deionised water to a depth of 1m. The length of the straight sections is 5 m (Fig. 1), while the bends have a radius of 0.5 m. The water flow is driven by two slow moving impellers (Type: EMU TR 14.145-4/6, WILO EMU GmbH) that drive the liquid at velocities between 0.01 and 1.0 m s<sup>-1</sup>. Note that the channel is expanded to 0.2 m in order to accommodate the pumps. The walls are constructed from 30 mm thick Plexiglas.

### 2.2 Measurement techniques

The measurements can be split into two groups, the measurements determining the observed velocities and the assessment of the distribution of the fibre agglomerates.

Three types of velocity measurements have been performed; these are ultrasound velocimetry, laser Doppler anemometry and particle image velocimetry. The ultrasound, US, velocimetry (FLUXUS® ADM-6725, Flexim GmbH) is used to determine the horizontal velocity of the fluid in the channel to ensure that the impellers are operated at the desired frequency. Field measurements of velocity using the ultrasound velocimetry sensors have also been performed in single-phase tests. Point-wise profile measurements over the channel height and width were also performed for single-phase flow using laser Doppler anemometry, LDA (LDV 380 - continuous wave laser of wavelength 815 nm and 40mW power with LDE 320 Laser-Driver + Photo-Multiplier, Polytec GmbH). Partial two-component velocity fields were also obtained by particle image velocimetry (PIV). The images examined the effect of the fibre accumulation between two weirs on the flow field in the lower region of the channel. The weirs were approximately 2m upstream of the origin. A 532 nm wavelength laser pulse

that gives visible green light is produced by the double pulse Nd: YAG-Laser (Neodym Yttrium-Aluminium-Granite). The pulse energy was 200 mJ, the diameter was 5.5 mm and the repetition rate was 15 Hz. The laser (New Wave Gemini 200-15, New Wave Research, Inc.) provides a light sheet to perform measurements of the flow field using particle image velocimetry. The particle image velocimetry was achieved by using 8-bit greyscale CMOS camera (MC1301 camera of Mikrotron GmbH) with a resolution of 1280 by 1024 Pixels at a frame rate up to 100 frames per second. The unmagnified pixel size is 12  $\mu\text{m}$  by 12  $\mu\text{m}$ .

Laser sensors (LV-H300 laser with LV-50 Amplifier, Keyence) and particle imaging detect the absence or presence of fibre agglomerates in the measurement locations in the channel. Images of the fibres obtained by a second MC1301 camera were of a whole segment of the channel. A small portion of the channel with a macroscopic lens of the channel was also used. The laser detection sensors (30 mm wide narrow beam of red light, with wavelength 650 nm, energy 3 mW and 3.5 ms pulse duration) were mounted perpendicularly to the flow at four channel heights,  $h \in (0.1 \ 0.2 \ 0.3 \ 0.4)$  m, on the impeller side of the channel 3 m upstream of the origin.

### 2.3 Experimental Uncertainty

The key uncertainties lie within the variability of the fibre agglomerate phase. The variability is attributed to agglomerate size, shape, compactness and convexity. The particle sizes in the sedimentation experiments in the channel are unknown and the description may differ significantly from previous assessments of the fibre agglomerates distributions (Krepper et al. 2009). The quantity of fine grain particles released by interactions with steam and the flow structures in the channel experiment or within the containment is also an unknown. This may have a significant impact on the mass of agglomerates that are transported in the channel. Note that the fine grains, which are formed during insulation material production, can comprise of up to 30% of the material. Therefore, the fine grain particles can significantly affect the quality of the phase definitions applied to the simulations.

The experimental techniques used to determine the distribution of the fibre agglomerates via laser detection measurements and particle imaging in the channel have a number of uncertainties. These include how the laser detection sensors are calibrated against the concentration of fibre agglomerates in the channel, the influence that the different agglomerates have on the laser signal and the variation of the fibre agglomerate distribution over the 0.1 m width of the channel. This last uncertainty affects both the laser detection sensors and the particle imaging, as one agglomerate could obscure other agglomerates passing the measurement region. Note that the number of laser detection sensors that have been used might be insufficient to describe the phenomena occurring in the channel, particularly in and above the boundary layer where strong changes in the fibre agglomerate concentration need confirmation.

### 2.4 Operational Mode

The racetrack channel can be operated in several modes. The addition of baffles can lead to situations where suspend fibre agglomerates can accumulate in the dead zones. However, the aim of the studies described here is to separate the effects of sedimentation and suspension into two distinct modes:

- *Suspension* examines the transport of 0.4417 kg of fibre agglomerates at an average velocity of 0.5  $\text{m s}^{-1}$ . Note that the height of the impellers was 0.33 m and 0.66 m. The measurement techniques included laser detection sensors, particle imaging in the boundary layer and ultrasound velocity measurements. Steam-blasted MDK was selected as the source for the fibre agglomerates.
- *Sedimentation* examines the transport of 0.0219 kg of fibre agglomerates held in a volume of 0.001  $\text{m}^3$  that is dropped into channel operating at velocities up to 0.2  $\text{m s}^{-1}$ . The agglomerates are dropped into channel on the side opposite to the impellers from a 0.44 m long tray, which 3.14 m from the origin given in Fig. 1. Note that the height of the impellers was 0.305 m and 0.68 m. The measurement techniques applied were particle imaging and ultrasound velocimetry. Steam-blasted MDK was selected as the source for the fibre agglomerates.

### 3. NUMERICAL MODELS

Different aspects of the numerical models, conditions and geometries used to resolve fibre agglomerate transport in the racetrack channel are described in the following subsections.

#### 3.1 Hydrodynamic model

A multi-fluid model is used to determine the transport of the fibre agglomerates, which are treated as dispersed fluids in the Eulerian reference frame (ANSYS 2009). Each phase considered has a set of mass and momentum conservation equations (Eqns. (1) and (2)) with additional internal and external forces that estimate the influence that each phase has on one another. The volume fraction is resolved by the limit given in Eqn. (4). A constraint that the pressure is shared by all phases is also applied.

$$\partial_t r_p \rho_p + \partial_j r_p \rho_p U_{j,p} = S_{j,p}^{MS} + \sum_{p=1}^{N_p} \Gamma_{j,cp}^{MS} \quad (1)$$

$$\partial_t r_p \rho_p U_{i,p} + \partial_j [r_p \rho_p U_{i,p} U_{j,p} + r_p \tau_{ij,p}] = S_{i,p}^M + M_{i,p}^M + \sum_{p=1}^{N_p} (\Gamma_{i,cp}^M U_{i,c} - \Gamma_{i,pc}^M U_{i,p}) \quad (2)$$

$$\tau_{ij,p} = p'_p \delta_{ij} - 2\mu_{eff,p} e_{ij,p} = p'_p \delta_{ij} - 2\mu_{eff} [0.5(\partial_j U_{i,p} + \partial_i U_{j,p})] \quad (3)$$

$$\sum_{p=1}^{N_p} r_p = 1 \quad (4)$$

Where  $t$  is the time,  $U_{i,c}$  is the  $i$ th velocity component of the continuous phase,  $U_{i,p}$  and  $U_{j,p}$  are the  $i$ th and  $j$ th velocity components of the  $p$ th phase,  $r_p$  is the  $p$ th phase volume fraction and  $\rho_p$  is the  $p$ th phase density.  $S_{j,p}^{MS}$  and  $S_{i,p}^M$  are the sum of all body forces in the mass and momentum conservation equations.  $M_{i,p}^M$  is the sum of all of the external source terms in the momentum conservation equation.  $\Gamma_{j,cp}^{MS}$ ,  $\Gamma_{i,cp}^M$  and  $\Gamma_{i,pc}^M$  are the interphase exchange term between phases  $c$  and  $p$  and vice versa.  $\tau_{ij}$  is the stress tensor,  $p'_p$  is the  $p$ th phase modified pressure and  $e_{ij}$  is the strain rate tensor.  $\mu_{eff,p}$  is the sum of the dynamic and turbulent viscosities.

#### 3.2 Interfacial Forces

Three interfacial forces are considered significant. These are the buoyancy force,  $S_p^B$  (Eqn. (5)), the drag force (Eqn. (6)),  $M_{i,p}^D$ , and the turbulence dispersion force (Eqn. (7)),  $M_{i,p}^{TD}$ , while the lift, wall lubrication and the virtual mass forces are assumed to have a negligible effect on the fibres. The solids particle collisions model and any agglomeration, erosion or breakage of the fibre agglomerates are not accounted for in the current model. Such models require a more detailed empirical knowledge of the particles and their behaviour with respect to the restitution coefficient, the compaction and elasticity moduli, their interactions with fluid turbulence and other agglomerates.

$$S_p^B = g_j r_p (\rho_p - \rho_c) \quad (5)$$

$$M_{i,p}^D = C_{i,cp}^D (U_{i,p} - U_{i,c}) \quad (6)$$

$$M_{i,p}^{TD} = C_{TD} C_{i,cp}^D \mu_{ic} (\rho_c \sigma_{ic})^{-1} (r_p^{-1} \partial_i r_p - r_c^{-1} \partial_i r_c) \quad (7)$$

$$C_{i,cp}^D = \frac{4}{3} \frac{C_{D,SN}}{d_p} r_p \rho_c |U_{i,p} - U_{i,c}| \quad (8)$$

$$C_{D,SN} = \begin{cases} 24 Re_p^{-1} & Re_p \ll 1 \\ 24 Re_p^{-1} (1 + 0.15 Re_p^{0.687}) & 1 < Re_p < 10^3 \\ 0.44 & 103 < Re_p < 2 * 10^5 \end{cases} \quad (9)$$

$$Re_p = d_p U_p \rho_c \mu_c^{-1} \quad (10)$$

Where,  $g_j$  is the acceleration due to gravity,  $\mu_{ic}$  is the continuous phase turbulent viscosity,  $\rho_c$  is the continuous phase density and  $\sigma_{ic}$  is the turbulent Schmidt number. The momentum exchange coefficient,  $C_{i,cp}^D$  (Eqn. (8)), is applied to both the drag (Eqn. (6)) and turbulence dispersion (Eqn. (7)) forces. In the simulations described here,  $C_{TD}$  is a constant with a value of 1. The ratio  $\mu_{ic} (\rho_c \sigma_{ic})^{-1}$

Phase	Description	$U_{j,up}$ (mm s <sup>-1</sup> )	$d_p$ (mm)	$\rho_p$ (kg m <sup>-3</sup> )	$\mu$ (kg m <sup>-3</sup> )	$\zeta_p$	$r_p$	$r_{p,in}$
$pF$	Fine fibre agglomerate	~0.5	0.5	1002	$\mu_c\mu_r$	0.0166	0.0626	-
$pL$	Light fibre agglomerate	~20	5	1002	$\mu_c\mu_r$	0.0166	0.0626	-
$pH$	Heavy fibre agglomerate	~50	5	1027	$\mu_c\mu_r$	0.0028	0.0104	0.6636
$c$	Continuous water	-	-	997	$8.899*10^{-4}$	-	$1-r_{pX}$	$1-r_{pH}$

Table 1: Phase properties and fractions.

defines the dispersion coefficient of the volume fraction gradient in Eqn. (7) the product of which gives the diffusion velocity of the dispersed phase. The fibre agglomerates are assumed to have the form of wetted spherical particles with the diameter,  $d_p$ . The drag coefficient,  $C_{D,SN}$ , was estimated using the Schiller-Naumann correlation given in Eqn. (9), where  $Re_p$  is the particle Reynolds number and  $\mu_c$  is the dynamic viscosity of the continuous phase.

### 3.3 Turbulence Model

The SST or Shear Stress Turbulence transport model of Menter (1994) was applied to continuous phase with automatic wall functions. Simulations applying different turbulence models to the channel section mesh have shown that the use of automatic wall functions with the  $k-\omega$  type of turbulence models can adequately model the flow in the near-wall region. The aim of such models is to approximate the Reynolds stresses, a flow phenomenon, by assuming a linear relationship with strain rate tensor. The turbulence viscosity is the coefficient in this relationship and it links the turbulence models to the momentum equations of both phases via the terms  $\mu_{eff,p}$  and  $M_{i,p}^{TD}$ . The turbulent viscosity of the dispersed and continuous phases are determined by the zero-equation model (Eqn. (11)) and the SST model (Eqn. (12)). Two transport equations are used estimate the turbulent viscosity in the SST model, which resolve turbulent kinetic energy,  $k_c$ , and the turbulent eddy frequency,  $\omega_c$ .

$$\mu_p = \rho_p \mu_c (\rho_c \sigma_{ic})^{-1} \quad (11)$$

$$\nu_{ic} = \mu_c \rho_c^{-1} = \alpha_1 k_c \left[ \max(\alpha_1 \omega_c, \sqrt{2e_{ij,c}e_{ij,c}} F_2) \right]^{-1} \quad (12)$$

$F_2$  is the second of blending functions, which is applied to Eqn. 12. The blending functions enable the switch between two forms of the turbulence transport coefficients. Coefficients (e.g.  $\alpha_1$ ) with the subscript 1 can adequately model the near wall region, while coefficients with the subscript 2 can model the free-stream turbulence well. Note that the standard implementation of SST model in ANSYS CFX is used here (ANSYS 2009).

### 3.4 Phase Description

Three dispersed phases were defined according to the terminal velocities (Eqn. (13)) of the fibre agglomerates by selecting the most frequent particle size and the agglomerate fibre density (Table 2). The terminal settling velocities,  $U_{j,sp}$ , of the fibre phases,  $r_{pL}$  and  $r_{pH}$ , were selected by two characteristics velocities. The  $r_{pH}$  phase was defined from the terminal velocity at which 80 % of fibre agglomerates have a smaller terminal velocity. The  $r_{pL}$  corresponds to the most frequently observed terminal velocity of the particles.

$$U_{j,sp} = \frac{4}{3} g_j \frac{\rho_p - \rho_c}{\rho_c} d_p \frac{1}{C_D} \quad (13)$$

The particle sizes for the  $r_{pL}$  and  $r_{pH}$  were determined from the mode of the MD2 agglomerate size and velocity distribution using Eqn. (13) to obtain the density (Krepper et al. 2009). The  $r_{pF}$  phase is defined with a diameter that is a tenth of the  $r_{pL}$  phase and it is assumed to have the same density of the  $r_{pL}$  phase. The  $r_{pF}$  phase is intended to represent the fibre agglomerates, which are formed in the channel due to agglomerate breakage and erosion caused by turbulence and impeller impacts.

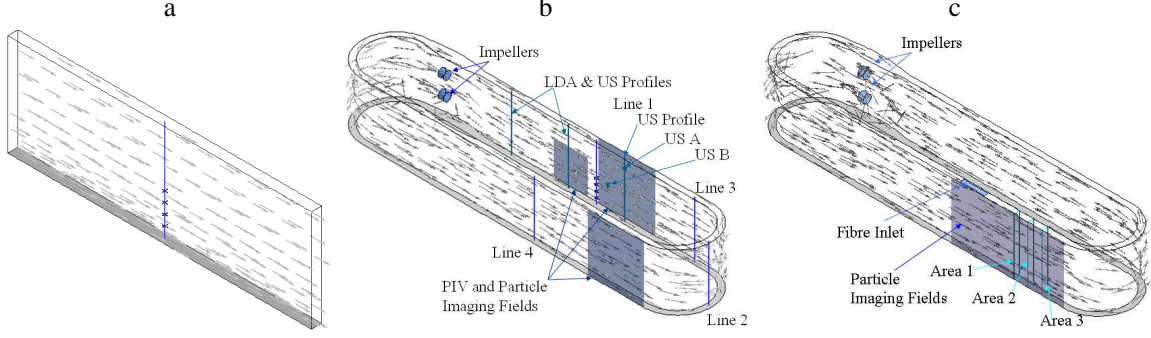


Fig. 2: Channel geometries, where the crosshairs indicate the laser detection sensors; a) Suspension section, b) whole channel for suspension, c) whole channel for sedimentation.

The relative viscosity,  $\mu_r$ , is given by correlation Eqn. (14) of Batchelor (1977) and it is used to calculate the mixture viscosity,  $\mu_m$ , via the product  $\mu_c \mu_r$ . The fibre share (Eqn. (15)) is based on an individual fibre density,  $\rho_f$ , of  $2800 \text{ kg m}^{-3}$  and the density of water, which is the continuous phase in the cases considered here. The fibre share indicates that the majority of the wetted agglomerate mass is water.

$$\mu_r = 1 + 2.5r_p + 7.6r_p^2 \quad (14)$$

$$\zeta_p = (\rho_p - \rho_c)(\rho_f - \rho_c)^{-1} \quad (15)$$

The volume fraction,  $r_p$ , for the simulations with one dispersed phase were estimated from the mass of fibre agglomerates added to the channel using Eqn. (16), where  $V_{ch}$  is the volume of the channel ( $1.4 \text{ m}^3$ ). Values of the volume fractions used are also given in Table 1. The volume fraction applied to the inlet condition of the sedimentation case corresponds to value given in the column  $r_{p,in}$  of Table 1. The mass of dry fibres,  $m_{p,dry}$ , corresponded to the respective experiments, where the suspension simulations applied a mass of  $0.4417 \text{ kg}$  and the sedimentation simulations applied a mass of  $0.0219 \text{ kg}$ . Note that the fibre material is based on steam-blasted MDK.

$$r_p = m_{p,dry}(\rho_p - \rho_c)V_{ch}^{-1} \quad (16)$$

### 3.5 Geometries and boundary conditions

The geometries used in the numerical models of the channel are depicted in Fig. 2 and details of the mesh resolution are given in Table 2. Three geometries are considered in the simulations described here. They are:

- The suspension section, which is a  $3 \text{ m}$  long by  $1 \text{ m}$  high section of the channel located upstream of the impellers. Note that the blue line in Fig. 2a is intended to correspond to Line 1 in Fig. 2b. Uniform inlet and outlet conditions applied to the variables  $U_{i,c}$ ,  $U_{i,p}$  and  $r_p$ . The initial conditions correspond to the inlet and outlet boundary conditions. The mean velocity applied to velocity component,  $u_i$ , of the inlet and outlet conditions of both phases was  $0.5 \text{ m s}^{-1}$  with a low intensity turbulence condition for the continuous phase. This gave a channel

Mesh	Total Nodes	Wall	$i$		$j$		$k$	
			Min	Max	Min	Max	Min	Max
Susp., section	767052	-	0.01	-	0.004167	0.0196	0.004	-
Suspension, whole channel	633434	Bends	0.036	0.043	0.01	0.01	0.01	-
		Sides	0.032	0.04	0.01	0.01	0.01	-
		Impellers	0.025	0.035	0.00835	0.0115	0.01	0.0233
Sedimentation, whole channel	812036	Bends	0.036	0.043	0.001	0.012	0.001	0.005
		Sides	0.026	0.044	0.001	0.012	0.001	0.005
		Impellers	0.018	0.034	0.001	0.012	0.001	0.005

Table 2: Mesh resolution of each mesh at the specified flow conditions.

Reynolds number (Coulson et al. 1990) of  $1.02 \times 10^5$ . The volume fractions applied correspond to values of  $r_p$  given eighth in column of Table 1. The side and base walls are no-slip walls and the top surface is a free-slip wall.

- The whole channel, which models suspension, applies the basic dimensions of the experimental channel (Fig. 1) with two cylindrical sub-domains (diameter of 0.14 m and length 0.1 m). The sub-domains are used to apply momentum sources at the heights of 0.33 m and 0.66 m in the parabolic section (Fig. 2b). A momentum source of  $6772 \text{ kg m}^{-2} \text{ s}^{-2}$ , which was estimated from the head loss over the channel length via the Darcy-Weisbach equation (Coulson et al. 1990), was applied to the continuity equation. The initial volume fractions, base, side and top wall conditions correspond to the equivalent conditions described for suspension section simulations. Note that lines 1 and 4 are located at  $(i, k) = (3.00, \pm 0.55) \text{ m}$ , line 2 is found at  $(i, k) = (5.55, 0.00) \text{ m}$  and line 3 is located at  $(i, k) = (4.75, -0.55) \text{ m}$ .
- The whole channel, which models sedimentation, is depicted in Fig. 2c. The geometry varies from the suspension simulations through the use of different impeller heights (0.305 m and 0.68 m) and an inlet condition on the +k side at 3.14 m from the channel origin. The momentum sources applied to the impeller sub-domains were adjusted to  $1290 \text{ kg m}^{-2} \text{ s}^{-2}$  to give a mean velocity of  $\sim 0.2 \text{ m s}^{-1}$ . The remaining conditions are no-slip walls applied to the base and sidewalls of the channel and a free-slip condition is applied to the top surface for the single-phase case. The top surface conditions are defined as velocity inlet conditions for the transport of a fibre agglomerate slug through the channel. The conditions are based on the addition of 1.1 litres of water containing 21.9 g of fibres to the channel through the 0.44 by 0.08 m boundary condition. The fibre-water mixture is dropped from a shallow rectangular tray, which is approximately 20 cm above the liquid level. The velocity at the fibre inlet was estimated assuming a perfectly inelastic collision as  $2.083 \text{ m s}^{-1}$ , with the fibre volume fraction given in ninth column of Table 1 for a period of 0.015 s, whilst the velocity and the fibre fraction at the remainder of top surface were both defined as 0 with a zero gradient turbulence condition. Three 20 mm wide analysis regions (Areas 1 to 3) are positioned downstream of the inlet condition beginning at 4.0995, 4.34825 and 4.597 m from the channel origin.

### 3.6 Solution techniques

The solution techniques applied to all three configurations included the definition of the initial static pressure as  $g_j \rho_c h$ , where  $h$  is the vertical distance and the use of the high-resolution mode of the solver for the advection and turbulence numerics schemes (ANSYS, 2009). Multiphase flow models were resolved using coupled equations with a correction step and volume-weighted body forces (ANSYS, 2009). The solution techniques, which varied according to the geometries and phenomena considered, are listed below:

- *The suspension section* is modelled in the steady state mode. Each case is initialised with the uniform inlet conditions. Note that  $j$  and  $k$  component velocities of the phases were initialised with velocities of  $1 \times 10^{-2}$ ,  $2 \times 10^{-2}$  and the turbulence parameters were automatically generated. A physical timescale of 0.1 s was used. The solution was left to converge until the root-mean-square residuals of the velocity components were less than  $10^{-6}$ .
- *The whole channel, which models suspension*, was resolved in two steps to aid convergence:
  - A steady single-phase step was run to provide a converged flow field. A physical timescale of 0.01 s was used. The flow field was initialised with zero velocity conditions and automatically defined turbulence parameters. Note that the solution was left to converge until the maximum residuals were less than  $10^{-4}$ .
  - A steady dispersed phase step was then run to model the distribution of fibre agglomerate phase about the channel. The cases were initialised by an interpolation of the single-phase flow field. A physical timescale of 0.005 s was used. The high-resolution scheme for Rhie-Chow velocity-pressure coupling was applied. Note that both these specifications were used to avoid numerical instabilities in the momentum and mass fraction equations. The solutions were considered converged once a stable

Mesh		Single phase max $y^+$				
		Impeller Segment	-i Bend	+k Straight	+i Bend	-k Straight
Suspension, channel section	Base	-	-	-	-	118
	Sides	-	-	-	-	114
Suspension, whole channel	Base	207	446	352	275	273
	Sides	519	577	456	283	288
Sedimentation, whole channel	Base	8	22	15	13	13
	Sides	34	34	22	14	15
	Impellers	177	-	-	-	-

Table 3: Mesh resolution and max  $y^+$  values at the specified flow conditions.

distribution of the fibre agglomerate volume fraction was achieved. This was considered acceptable when the variation in the volume fraction at the monitor point with the largest respective value was less than  $\pm 3\%$  over several thousand iterations or when the maximum residuals were less than  $10^{-4}$ .

- *The whole channel, which models sedimentation* was resolved in a transient approach due to the experiments performed. Note that the second order backward Euler scheme was used to progress the solution through time. The simulations were performed in two steps:
  - The single-phase transient step resolved the transport of water through the channel for 400 s or approximately 5 circuits of the channel. The flow field was initialised on a coarse mesh version of the mesh (367372 nodes) depicted in Fig. 2c with zero velocity conditions and automatically defined turbulence parameters. After 150 s, the flow field from the coarse mesh was used to initialise the final mesh by interpolation. Each time step was considered converged when the maximum residuals of the momentum equations were less than  $10^{-4}$ . Note that adaptive time stepping was used to increase the time-step size from 0.005 s to 0.05 s during the course of the simulation. The largest time step size used gave a maximum Courant number of 7.
  - The dispersed phase transient step modelled the transport of a slug of fibre agglomerates from the inlet for 10 s. Two time step sizes were used with 0.0025 s for the first 0.499 s and 0.005 s for the remainder of the simulation. Each time step was considered converged when the root mean square residuals of the momentum equations were less than  $10^{-4}$ . The maximum Courant number was of the order of 1 throughout the simulation.

### 3.7 Numerical Uncertainties

The key uncertainties in the numerical model are that only a single agglomerate size, density and shape is considered in each case. Experiments show a range of agglomerate sizes, shapes and densities, which may undergo flocculation, erosion and breakage.

The velocities considered in the suspension experiments are far away from the velocities ( $< 0.2 \text{ m s}^{-1}$ ) that occur in the containment sumps of both boiling and pressure water reactors. The key reason behind the selection of such a high velocity are that it is necessary to determine what phase definitions lead to the suspension of the fibre agglomerates, at conditions where experiments show them to be suspended. The consequences of the high velocity are that lower concentrations are observed, which leads to lower mixture viscosities and lower collision frequencies and lower rates of flocculation. Any fibre agglomerates that undergo erosion and breakage should have already done so at the velocities considered, though this needs experimental confirmation. Note that the velocity condition applied to fibre inlet condition for the simulation of sedimentation in the whole channel might be inaccurate, as momentum could be lost from the falling liquid volume as it hits the liquid surface.

Finally, the resolution of the grid in the boundary layer is also significant as the channel width is small. The  $y^+$  values in Table 3 indicate that the mesh is adequately resolved near to the wall for the suspension section and whole channel simulations for sedimentation when the SST model is applied

with automatic wall functions. The  $y^+$  values for whole channel suspension show that the mesh is coarse, due to the long simulation times required to achieve a steady state. Finer meshes may cause a vertical shift in the resolved volume fraction profiles. In the case of the sedimentation simulations, thin wall conditions were applied to the impeller sub-domains in order to avoid instabilities in the bend downstream of the impellers. Best practice guidelines concerning the mesh resolution will be followed once appropriate phase definitions are defined and further experimental investigations have been performed for the suspension of the dispersed phase. Nevertheless, the scale of the containment sump of an NPP is considerably larger than the simulations performed here.

## 4. RESULTS

The following subsections split the experiment and numerical results into the studies on the transport of the suspension through the channel and the sedimentation of a known mass of fibre agglomerates.

### 4.1 Suspension

This section describes the results obtained by the experiments and simulations performed to examine the suspension of a known mass of fibre agglomerates in the horizontal flows found in the racetrack type channel. The plots presented in Fig. 3a-c depict the signals obtained by the laser detection sensors and the variation in the signal output ( $V'$ ) with channel height. The signal outputs were normalised by Eqn. (24), where  $(V'_{max} - I)$  is the maximum value of the traces subtracted by the minimum signal output in Fig. 3a. Note that the traces obtained by two ultrasound velocimetry sensors indicate the velocities observed in the channel during the experiments.

$$V'' = I - (V'_{max} - I)^{-1}(V' - I) \quad (17)$$

The distribution of the fibre agglomerates over the four measurement locations are given in Fig. 3b-c.

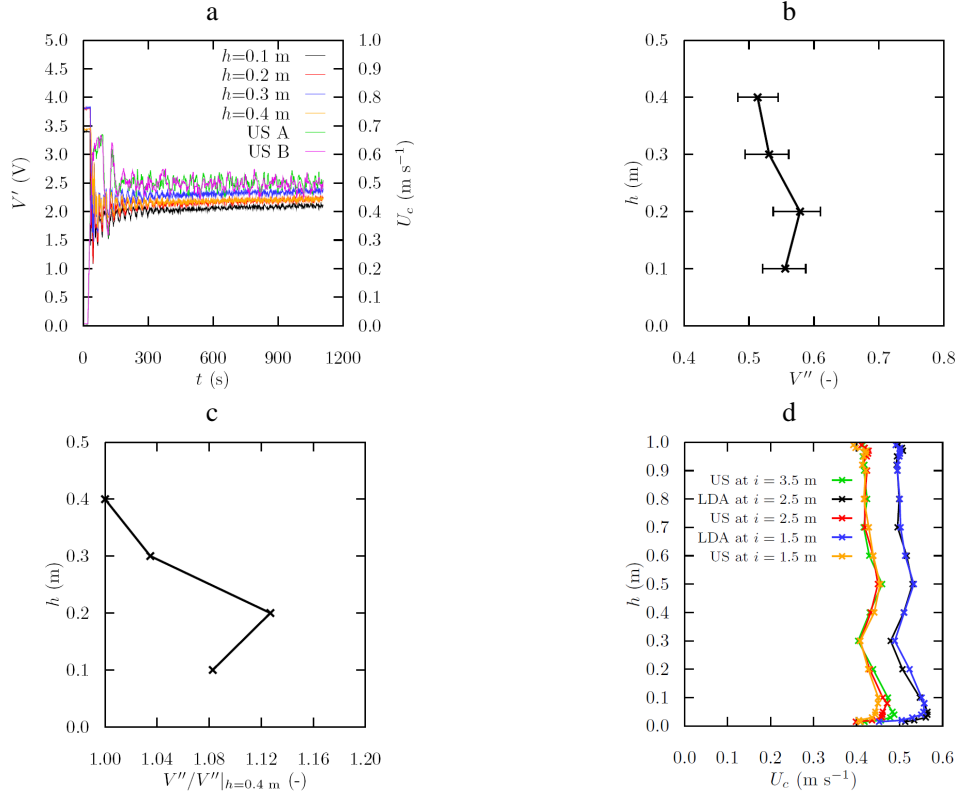


Fig. 3: Experimental measurements. a-c) Laser detection sensors output for the fibre agglomerate distribution (0.44 kg of steam blasted MDK); a) Signal output with ultrasound velocity measurements, b) normalised signal output, c) Ratio of the normalised signal output to the normalised output at 0.4 m; d) LDA and US profiles of single-phase velocity on the  $-k$  channel side.

The variation of both  $V''$  and  $V''/V''|_{h=0.4m}$  indicates that the concentration of the fibres increases at a height of 0.2 m, which is just outside of the boundary layer. The velocity profiles given in Fig. 3d obtained by LDA and US measurements at a similar impeller operating condition for single-phase flow have two peak regions, one near to the middle of the channel and one near to the channel base, which corresponds to the edge of the boundary layer. The accumulation of fibres between 0.1 and 0.3 m, where a 12 % change in the laser detection signal was observed corresponds to a fluid layer where the velocity gradient is greater than the fluid layer directly above the boundary layer. However, the influence that the flow field has on the fibre agglomerate flux requires further confirmation. Note that there is an unexplained apparent difference of  $0.1 \text{ m s}^{-1}$  between both types of velocity measurements for both profiles where a direct comparison can be made ( $i = 1.5$  and  $2.5$  m upstream of the origin).

Profiles from the suspension section simulations are depicted in Fig. 4. The volume fraction of  $pH$  and  $pL$  phases increases to values in excess of 0.5 over the lowest 0.02 m of the channel, which corresponds to the lower wall boundary layer where strong velocity gradients (Fig. 4c). This is not the case for the  $pF$  phase, where the change in the volume fraction is small over the whole channel height (Fig. 4a-b). Thus, the  $pF$  phase is comparable with the experiments in boundary layer region where no fibre agglomerates accumulated at the velocity considered. Note that the mass of loose fine grain particles is not considered in the simulations, which make up to 30 % of the insulation material; thus, this could affect the concentrations of the fibre agglomerates observed in both the experiments and the simulations.

Nevertheless, the uniform velocity profile (Fig. 4c) in the free-stream region of the channel results in the uniform distribution of the fibre agglomerates for all the dispersed phases considered (Fig. 4a-b). This uniformity was not observed to experiments, where a change of 12% of the laser detection signal was observed. Note that the upper interface of the fibre agglomerate flux differs for each phase, where the  $pH$  phase has the greatest reduction in height, the  $pF$  shows little no or deviation from the free-slip surface and the upper interface of the  $pL$  phase flux occurs between that of the  $pF$  and  $pH$  phases.

Therefore, as flow structures that have been shown to affect the fibre agglomerate flux in the channel it became necessary to replicate such flow structures, which could only be obtained by modelling the whole channel. Fig. 5 gives profiles of the volume fraction, volume fraction ratio and the velocity. The volume fraction profiles in Fig. 5a-b show that the  $pF$  phase corresponds well with the variations observed in the laser detection signal. The  $pL$  phase is also affected by the flow field; however, the variation is 60 times greater than the  $pF$  phase. The  $pH$  phase settles to the bottom of the channel. Note that higher resolution simulations may show a reduction in the volume fraction at heights for  $h < 0.2$  m for the  $pF$  phase on line 1; however, these simulations have not yet been performed due to lack of available simulation time.

The velocity profiles in Fig. 5c and Fig. 5f show that the flow structures, which influence the volume fraction profiles on line 1 may originate from flow instabilities in the second +i bend. However,

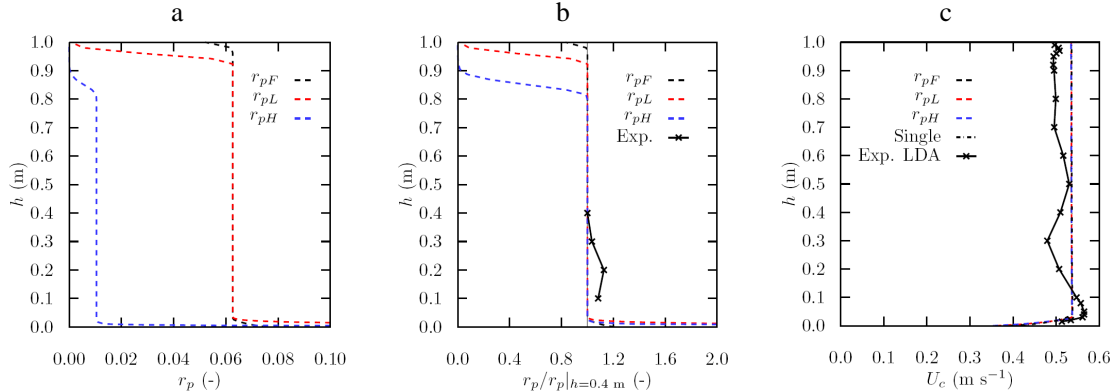


Fig. 4: Profiles from the suspension section simulations; data from the line in Fig. 2a: a) Volume fraction of the fibre agglomerate phase, b) Ratio of the volume fractions of fibre agglomerate phase to its value at 0.4, c) Velocity magnitude of the continuous phase

experimental confirmation of the fibre distribution and velocity profiles on the +k side of the channel is required to confirm the profiles observed in the simulations. The velocity profiles also show that the mesh used here adequately models the continuous phase flow field. Profiles of single-phase flow are also given for comparison in Fig. 5c and Fig. 5f between single-phase and multiphase flow and at different mesh resolutions. Note that the transient higher resolution (Single TH) case produced similar velocity profiles to steady state lower resolution case (Single SL), both for single-phase flow. Note that there are small deviations away from the profiles for the disperse phase cases, where only data from lines 1 and 2 are shown for reasons of clarity.

Further experimental measurements on both sides of the whole channel are needed to provide a better description of the fibre agglomerates that experience the flow conditions observed in the channel due to the previously described uncertainties in the experimental data.

## 4.2 Sedimentation

The sedimentation of a known mass of agglomerates in a horizontal flow was also examined experimentally and numerically in the racetrack type channel. Fig. 6 depicts the experimental and numerical traces of the fibre agglomerate fraction as well as images of the volume fraction obtained after 6 s of simulation time. Eqns. (25) and (26) were used to estimate the fraction,  $\chi$ , of the Areas 1-3 indicated in Fig. 2c occupied by the fibre agglomerate phase, where  $N$  is the number of pixels and  $V$  the volume of each measurement area,  $a$ , which is occupied by the fibre agglomerates with a volume fraction greater than 0.01.

$$\chi_{exp} = N_{a\chi,p} / N_{aT} \quad (18)$$

$$\chi_{sim} = V_{a\chi,p} / V_{aT} \quad (19)$$

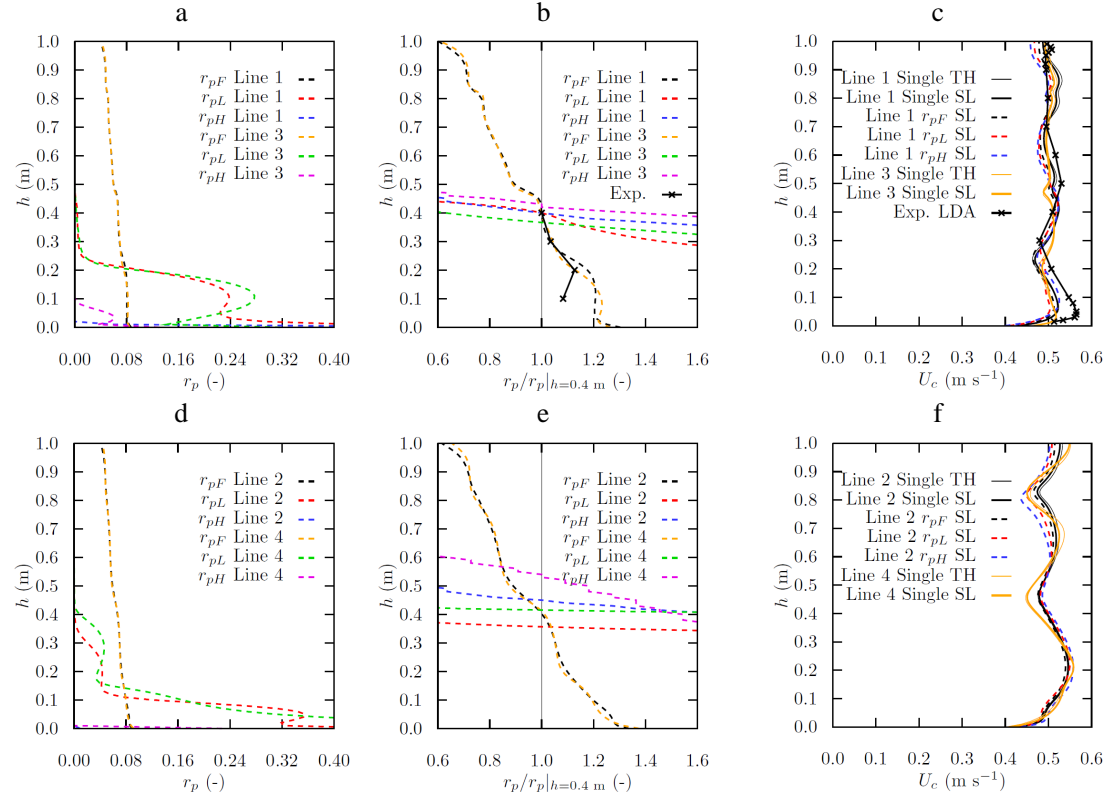


Fig. 5: Profiles of the whole channel simulations of suspension; Data obtained from lines 1 and 3 in Fig. 2b: a) Volume fraction of the fibre agglomerate phase, b) Ratio of the volume fractions of fibre agglomerate phase to its value at 0.4, c) Velocity magnitude of the continuous phase. Data from lines 2 and 4 in Fig. 2b; d) Volume fraction of the fibre agglomerate phase, e) Ratio of the volume fractions of fibre agglomerate phase to its value at 0.4, f) Velocity magnitude of the continuous phase

The traces indicate that the movement of the fibre agglomerate phase matches the experiments well (Fig. 6a-c); however, the dispersion or spread of the agglomerates is much greater in the experiments than in the simulations (Fig. 6d-f). Note that in Fig. 6a-c & f, a mesh that had been locally refined in the streamwise direction is also depicted. The refined mesh shows similar dispersion properties with sharper peaks (Fig. 6a-c) and the overall shape of the fibre agglomerate slug is similar; however, the distribution of agglomerates differs (Fig. 6f). The reduced vertical dispersion maybe caused the range of agglomerate sizes present in the experiments leading to different settling velocities. Hindered settling may also influence the vertical spread of the agglomerates.

## 5. FURTHER EXPERIMENTAL INVESTIGATIONS

Due to the uncertainties from the measurements described here, further experimental studies of the suspension of the fibre agglomerates have been proposed. The studies will apply particle imaging and particle image velocimetry simultaneously to determine the influence that the particles have on the fluid phase. This would also include single-phase measurements of the velocity field with PIV. The influence that the fibre agglomerates have on the laser detection signal will also be analysed. More measurement locations will also be considered to help elucidate the influence of the flow on the fibre suspension. The mass of the loose fine grains also needs to be accounted for to give better phase definitions. The settling characteristics of the fibre agglomerates suspended in the channel also need determination.

## 6. CONCLUSIONS

Simulations of fibre agglomerate suspension and sedimentation have been performed on a racetrack type channel. The sedimentation simulations physically agree with experiments performed, while the suspension simulations show good quantitative agreement with available experimental data. However, further improvements are required for the experimental characterisation of the fibre agglomerate distribution for the appropriate validation of the numerical models and assumptions used here.

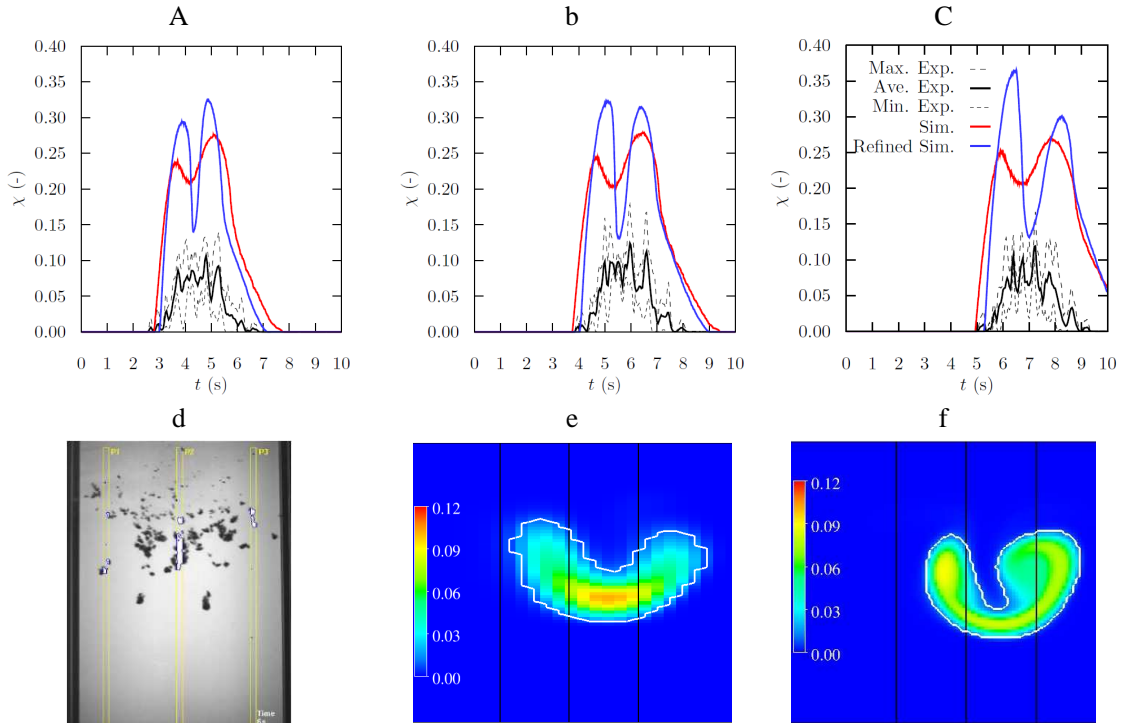


Fig. 6: Profiles and traces from the sedimentation studies; Experimental and numerical trace data from areas 1-3 in Fig. 2c: a) Area 1, b) Area 2, c) Area 3, the key is common to plots a, b and c; d) An photograph of MDK agglomerates after 6 s; e) & f) contours of volume fraction after 6 s at different mesh resolutions, where the white line indicates the extent of the agglomerate at  $r_p = 0.01$ ;

## ACKNOWLEDGMENTS

The reported investigations are funded by the German Federal Ministry of Economy and Technology under contracts No. 150 1270, 150 1307 and 150 1363.

## NOMENCLATURE

Symbol	Unit	Definition
$C$	-	coefficient
$d$	m	particle diameter
$e$	$s^{-1}$	strain rate tensor
$F_2$	-	second blending function of the SST model
$g$	$m\ s^{-2}$	acceleration due to gravity
$h$	M	channel height
$k$	$m^2\ s^{-2}$	turbulent kinetic energy
$M$	$kg\ m^{-2}\ s^{-2}$	external source terms
$m_{p,dry}$	kg	dry weight of the fibre agglomerates
$N$	-	number
$P$	$m^2\ s^{-1}$	turbulence production term
$p'$	$kg\ m^{-2}\ s^{-2}$	modified pressure
$Re$	-	Reynolds number
$r$	-	volume fraction
$S$	$kg\ m^{-2}\ s^{-2}$	body source term
$t$	s	time
$U$	$m\ s^{-1}$	velocity vector
$V$	$m^3$	volume
$V'$	V	laser detection signal output
$V''$	-	normalised laser detection signal output
$y$	m	distance to the nearest wall

Greek Symbols	Unit	Definition
$\alpha$	-	turbulence coefficient
$\Gamma$	$kg\ m^{-3}\ s^{-1}$	interphase exchange term
$\delta$	-	Kronecker's delta
$\mu$	$kg\ m^{-1}\ s^{-1}$	dynamic viscosity
$\nu$	$m^2\ s^{-1}$	kinematic viscosity
$\rho$	$kg\ m^{-3}$	density
$\zeta$	-	share of fibres in the wetted agglomerate
$\sigma$	-	turbulent Prandtl or Schmidt number
$\tau$	$kg\ m^{-2}\ s^{-2}$	stress tensor
$\chi$	-	fraction for the comparison of the sedimentation studies
$\omega$	$s^{-1}$	turbulent eddy frequency

Superscripts	Definition
$B$	buoyancy
$D$	drag
$M$	momentum
$MS$	mass
$TD$	turbulent dispersion

Subscripts	Definition
$l$	coefficients for the near wall region
$2$	coefficients for the free-stream region
$a$	Sedimentation measurement area
$c$	cth phase
$ch$	channel
$cp$	term acting between cth and pth phases
$eff$	effective
$F$	fine fibre agglomerate
$f$	individual fibre
$H$	heavy fibre agglomerate
$i$	ith direction component (transverse)
$in$	inlet condition
$j$	jth direction component (vertical)
$k$	kth direction component (spanwise)
$L$	light fibre agglomerate
$m$	mixture
$max$	maximum value
$p$	pth phase
$pc$	term acting between pth and cth phases
$r$	relative
$SN$	Schiller-Naumann
$sp$	terminal settling velocity of the fibre agglomerate
$T$	total
$t$	turbulent
$\chi$	volume occupied by fibre agglomerates

## REFERENCES

- ANSYS, *ANSYS CFX-12*, Ansys Inc., Canonsburg, PA, USA 2009.
- G. K. Batchelor, "The effect of Brownian motion on the bulk stress in a suspension of spherical particles", *Journal of Fluid Mechanics*, 83, 97-117 (1977).
- J. M. Coulson, J. F. Richardson, J. R. Backhurst, J.H. Harker, *Coulson & Richardson's Chemical Engineering, Volume 1, Fourth Edition* (pages 54, 69 & 77). Pergamon Press, Oxford & New York, 1990.
- H. L. Detar, D. T. McLaughlin, R. J. Lutz, "Probabilistic Model for debris-induced loss of long term core cooling", *Proc. of the 16th International Conference on Nuclear Engineering*, Orlando, Florida, USA, May 11-15, ICONE16-48780 (2008).
- E. Krepper, G. Cartland-Glover, A. Grahn, F.-P. Weiss, S. Alt, R. Hampel, W. Kaestner, A. Seeliger, "Numerical and experimental investigations for insulation particle transport phenomena in water flow", *Annals of Nuclear Energy*, 35, 1564-1579 (2008).
- J. I. Lee, S. J. Hong, J. Kim, B. C. Lee, Y. S. Bang, D. Y. Oh, B. G. Huh, "Debris transport analysis related with GSI-191 in advanced pressurized water reactor equipped with incontainment refuelling water storage tank", *Proc. of the XCDF4NRS Workshop - "Experiments and CFD Code Applications to Nuclear Reactor Safety"*, Grenoble, France, 10-12 September, AC-05 (2008).
- F.R. Menter, "Two-equation eddy-viscosity turbulence models for engineering applications", *AIAA-Journal*, 32(8), 1598-1605 (1994).
- K. M. Seo, C. H. Shin, W. T. Kim, J. P. Park, B. S. Han, "CFD Analysis on Debris Transport to the Containment Recirculation Sump for OPR1000 Plant", *Proc. of the 13th International Topical Meeting on Nuclear Reactor Thermal Hydraulics*, Kanazawa City, Japan, September 27-October 2, N13P1141 (2009).

**Relevant OECD and NUREG Reports**

Knowledge Base for Emergency Core Cooling System Recirculation Reliability, NEA/CSNI/R(95)11, 1996.

Knowledge Base for the Effect of Debris on Pressurized Water Reactor Emergency Core Cooling Sump Performance, NUREG/CR-6808; LA-UR-03-0880, 2003.

GSI-191: Integrated Debris-Transport Tests In Containment Floor Geometries, NUREG/CR-6773 LA-UR-02-6786, 2002.

Knowledge Base for Strainer Clogging -- Modifications Performed in Different Countries Since 1992, NEA/CSNI/R(2002)6, 2002.

Debris impact on Emergency coolant recirculation, Workshop Albuquerque, NM, USA February 2004, Proceedings OECD 2004 NEA No. 5468 (2004).